THE OHIO STATE UNIVERSITY - DEPARTMENT OF MECHANICAL AND AEROSPACE ENGINEERING

Evolution of Disturbances in the Boundary and Entropy Layers of Hypersonic Flow Over Blunted Flat Plates

---

Undergraduate Research Thesis

Presented in partial fulfillment of the requirements for Bachelor of Science in Aerospace Engineering with Honors Research Distinction for May 2019

By

Brandon Teitelbaum

Thesis Defense Committee:

Dr. Datta V. Gaitonde, Advisor

Dr. Clifford A. Whitfield

Abstract

Compared to laminar flow, turbulent flow causes significantly higher drag and heat transfer to an object in the flow, representing a major design challenge for all flight vehicles. This challenge is made only more difficult on hypersonic vehicles, for which drag and high temperatures are already of major concern. Laminar-turbulent transition is a complex process which can follow many paths. When freestream disturbances are small, transition of supersonic boundary layers on sharp plates has been shown to be the result of second-mode instabilities. As the leading edge is blunted, the transition location moves downstream, which is understood as a stabilizing effect on the second-mode instability. However, once a certain bluntness is reached, experiments have demonstrated the movement of the transition location back upstream, a phenomenon known as transition reversal. Reversal is not explained by the second-mode instability and no explanation for this phenomenon yet exists. The current project will serve as a building block for future work with the ultimate goal of demonstrating transition reversal and providing an explanation for this phenomenon. In order to achieve this goal, this project will first discuss results for the mean flow over a sharp plate. Then a technique for determining the most unstable frequency of disturbance at any location will be developed. This technique will be demonstrated on the sharp plate for which the most unstable frequency can be determined by Linear Stability Theory. In demonstrating the validity of this approach, the groundwork will be laid for applying this technique to two blunted plates for which Linear Stability Theory does not predict a reversal in the trend of the unstable frequencies. Base flow results for these two blunted plates will be discussed, while the application of the developed technique to the blunted plates is the subject of ongoing work. The ability to determine the most unstable frequency without Linear Stability Theory will provide a tool to validate LST results and provide insights into receptivity mechanisms to understand the system response to frequencies not predicted by Linear Stability Theory.

Dedication

This thesis is dedicated to my entire family for their love and support. To my parents Vicki and Michael, my sisters Lindsey and Ally, their husbands David and Evan, and my niece Callie who celebrates her first birthday on the day of the submission of this thesis.

Acknowledgements

I'd first like to thank Dr. Datta Gaitonde for welcoming me into his lab and serving as my advisor. I'd also like to thank Dr. Clifford Whitfield for serving on my defense committee for this thesis. This project couldn't have been completed without the contributions of Hemanth Goparaju and Unnikrishnan Sasidharan Nair. Thank you to both of them for their work on this project as well as their overall guidance in my research. I'd also like to recognize the support provided for this project by the Office of Naval Research (PO: R. Burnes and TPOC: E. Marineau). Computer time for this project was provided by the Ohio Supercomputer Center and post-processing was performed using FieldView by Intelligent Light.

Contents

List of Figures

1 Background and Introduction

Laminar flow is characterized by fluid motion which is highly ordered, whereas turbulent flow is characterized by chaotic, unsteady structures of different scales. Laminar flow is mostly well understood, while much less is known about the intricacies of turbulent flow. However, it is well known that turbulent flow causes much higher drag and heat transfer rates than laminar flow. Thus, there is great interest in the fundamental understanding, and hence control, of turbulent flows. Yet, the all-pervasive nature of turbulence and the lack of a unified theory has presented significant challenges to the study of turbulence. This has led fluid dynamicists for centuries to study the evolution of a flow from a laminar state to a turbulent one, known as transition. A general approach for the study of transition to turbulence usually begins with an instability wave in the laminar flow which grows and transitions the flow into another state. By studying these instabilities that cause transition, aerodynamicists can develop appropriate control techniques.

Osborne Reynolds first demonstrated the process of flow transition in 1883. Since then, fluid dynamicists have worked extensively to gain an understanding of the processes that cause transition. Generally, transition begins with a receptivity process where acoustic, vortical, or entropic disturbances in the freestream enter the boundary layer and generate unstable perturbations. Following receptivity, there are several different paths that a flow can take to turbulence depending on the amplitude of the initial disturbance, as demonstrated in Figure 1 (Morkovin, Reshotko, & Herbert, 1994). If the initial disturbances are small enough, path A in Figure 1 is followed. In this case, the growth of the disturbances is described by Linear Stability Theory (LST) of primary modes such as the well known Tollmien-Schlichting (T-S) wave. This primary mode growth is relatively weak. However, three-dimensional, non-linear secondary instabilities eventually take over causing faster growth rates and eventually lead to turbulence.

It is also possible that the initial disturbances are large enough that linear growth is bypassed, turbulent spots appear, and the flow quickly becomes turbulent. This process is represented by path E in Figure 1 and is known as bypass transition. Relatively little is known about bypass transition, as the process is highly nonlinear. However, it is generally accepted that bypass occurs when initial disturbance growth is not described by primary modes of the Orr-Sommerfeld Equation (Saric, Reed, & Kerschen, 2002).

When initial disturbance amplitudes are neither small enough to be described by LST or large

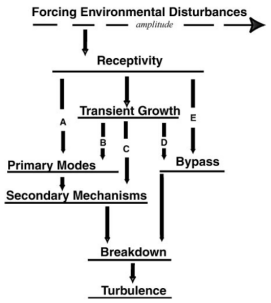

Figure 1: Paths to Turbulence

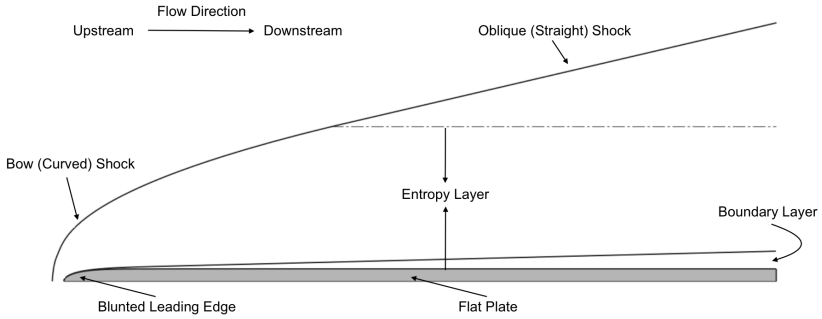

Figure 2: Important Flow Features

enough to cause bypass transition, the flow follows a transient growth path to turbulence. Transient growth occurs when two stable modes interact and experience some initial growth before decaying exponentially. Depending on initial disturbance amplitude, transient growth can be followed by primary mode growth, secondary instabilities, or direct bypass. These paths are shown in Figure 1 as paths B, C, and D, respectively. As with bypass transition, very little is known about the process of transient growth. Both of these areas remain major areas of study as a more complete understanding of transition mechanisms is developed.

Building an understanding of transition is further complicated when one begins to examine the transition of supersonic flows. When supersonic flow passes over the nose of a blunt object, a curved bow shock is generated in front of the nose of the object. Furthermore, as the flow passes through a bow shock, an entropy layer of rotational inviscid flow with non-uniform velocity and temperature distributions is formed. Simultaneously, a viscous boundary layer develops over the surface of the body. The formation of the bow shock, entropy layer, and boundary layer are demonstrated in Figure 2. It has been shown theoretically that a single entropic, acoustic, or vortical disturbance upstream of the bow shock will result in a disturbance of all three types downstream of the shockwave. (D'yakov, 1958).

Hypersonics refers to a special type of supersonic flows travelling several times the speed of sound, usually Mach 5 or above. Hypersonic flows experience all the challenges of supersonic flows, and yet are further complicated by several unique characteristics including extreme temperatures, real gas effects, finite rate kinetics, and thermal and chemical non-equilibrium. However, the study of hypersonics is vital to the design of viable high-speed flight vehicles. Hypersonic flight

vehicles span private, civilian, and military applications and include space exploration vehicles, high-speed commercial transport, and high-speed missiles and interceptors. In order to better design these high-speed flight vehicles, studies are done involving many relatively basic geometries and results from these studies can then be applied to the design of flight vehicles. Several such studies, specifically relating to transition reversal, are briefly reviewed in the following section.

1.1 Literature Review

The effect of the entropy layer on laminar-turbulent transition has been a major focus of interest since Brinich and others investigated the effect of leading edge bluntness on transition. Brinich showed for cones and hollow cylinders at Mach 3.1 that the transition location moves downstream with increasing bluntness (Brinich, 1956) (Brinich & Sands, 1957). This stabilizing effect was explained by Brinich as a result of the existence of the entropy layer over the surface of blunted objects. In 1967, Stetson confirmed that increasing bluntness does result in the movement of the transition location downstream, but only up to a certain point. After reaching some threshold value, it was observed that the transition location would begin moving back upstream (Stetson, 1967). This reversal is a phenomenon now known as the blunt body paradox, or transition reversal, and is the primary motivation of this thesis. Stetson's experiment involved various blunted cones at Mach 5.5. Just a year later, Softley demonstrated transition reversal on blunted cones at Mach 10 (Softley, 1968).

Since transition reversal was first demonstrated by Stetson, there have been many theoretical, experimental, and numerical studies which have attempted, with varying levels of success, to provide an explanation for this phenomenon. Several studies have attempted to show transition reversal as an effect of surface roughness, but much of the results did not support this explanation (Lysenko & Maslov, 1981) (Batt & Legner, 1983). In 2012, Lei carried out a linear stability analysis on the original case of Stetson (Stetson, 1967) and showed that LST predicts bluntness has a stabilizing effect on the 2^{nd} mode instability (Lei & Zhong, 2012). The 2^{nd} mode instability, or Mack mode, is well understood to be the primary instability in supersonic boundary layers. Thus, Lei showed that if only the 2^{nd} mode is considered as the instability causing transition, the location of transition would move continuously downstream with increasing bluntness, and no reversal would occur. As a result, some other instability must be causing transition to occur in the more blunt cases.

In 2018, Cook utilized an Input-Output Analysis to examine the problem of transition reversal

(Cook, Thome, Brock, Nichols, & Candler, 2018). It was observed that the entropy layer instability grows slowly for the case of the relatively sharp cone. However, for the more blunt case, the entropy layer instability grows much faster and can become large enough to trigger transition before the 2nd mode instability. Cook also observed that lower frequency waves are excited more with increasing bluntness, a trend that is in agreement with other observations of reversal. However, these results were only obtained by manually scanning the entire lower frequency range in order to determine the most unstable frequency, which is not ideal and also failed to give any insight into what was actually causing these low frequency unstable waves. It was also recently shown by Mortensen that in some cases, the supersonic mode, not the 2nd mode, may cause transition in flows at very high Mach numbers with large nose bluntness (Mortensen, 2018). Having summarized several previous studies relating to transition reversal, the focus of the current thesis is detailed in the next section.

1.2 Focus of Thesis

Despite the many attempts at studying the problem of transition reversal, there has yet to be a computational study which has clearly and definitively demonstrated reversal and provided an explanation for the cause of this phenomenon. One of the significant challenges to studying transition reversal has been determining the most unstable frequencies for supersonic flow over a blunt body. Identifying these unstable frequencies is an essential tool in the study of transition. For non-blunted objects, these frequencies can be obtained from LST. However, LST fails to accurately identify these unstable frequencies for cases involving blunt bodies, where a significant boundary and entropy layer both exist. Therefore, in order to properly study the problem of transition reversal, a new method for determining the most unstable frequencies in a flow must be developed.

This thesis will focus on developing and validating such a methodology in order to advance the study of transition reversal. Computational fluid dynamics (CFD) simulations will be utilized to examine viscous, hypersonic flow over various geometries. Base flow results will first be obtained and analyzed for the non-blunted plate. A Linear Stability analysis of the non-blunted plate will also be presented. Disturbances will then be added to the base flow of the non-blunted plate, and the evolution of these disturbances will be studied. A new methodology for determining the most unstable frequency will be developed. Specifically, this technique will utilize various types of random forcing in order to extract the most unstable frequency at a given location. This technique will be applied to a non-blunted plate in an attempt to validate the accuracy of this approach.

Validation will involve comparing the results from each type of forcing with each other as well as to results obtained from LST. The successful validation will pave the way for applying this technique to blunted plates for which LST fails to accurately provide the most unstable frequency. The foundation for applying this technique to blunted plates will be built in this project by discussing base flow results for two plates of differing bluntness. The addition of disturbances and the final application of this technique to blunted plates will be the subject of future writing.

More specifically, there are three goals which this thesis will focus on achieving. First, to develop a methodology to determine the most unstable frequencies without the use of LST. Then to validate this methodology by applying it to a non-blunted plate and comparing the results to those obtained from LST. Finally, to lay the groundwork for the application of this methodology to various blunted plates by studying results for the base flow over two different blunted plates.

1.3 Significance of Research

Overall, hypersonic transition is a focus of study in order to better inform the design of future hypersonic vehicles. Two of the bigger challenges in designing hypersonic vehicles are minimizing drag and minimizing heat transfer rates to the vehicle. Both of these challenges can be exacerbated by turbulent flow which results in higher drag and heat transfer to the surface compared to laminar flow. Therefore, if an understanding of the mechanisms that cause flow transition can be built, new vehicles can incorporate control techniques to suppress these mechanisms and delay transition to turbulence.

The current project will add to the understanding of hypersonic transition in several ways. First, this project will build the framework for demonstrating the phenomenon of transition reversal, which has only been partly demonstrated computationally to this point. In doing so, this project will provide a tool which will allow the most unstable frequency in a flow to be determined simply from the geometry and operating conditions. Such a tool is vital to the study of transition reversal and has several other potential applications throughout the field of stability analysis. Additionally, this project will attempt to gain new insight into the interaction between the boundary and entropy layers on a blunted plate by examining the base flows over a non-blunted plate and two different blunted plates.

1.4 Overview of Thesis

Following this introduction, the next chapter of this thesis will briefly describe the geometry of

specific flat plates chosen for this study. Then, the details of the meshing procedure for each of the chosen geometries will be discussed. Following that, the computational solver used in this project will be described and the boundary conditions for the solver will be defined. Base flow results for the non-blunted plate will then be discussed. Next, an LST analysis of the base flow for the non-blunted plate will be performed to determine the most unstable frequency at a given location, which will provide a baseline result to which results from the new methodology can be compared. The following chapter will lay out the specific methodology which was developed in order to extract the most unstable frequencies. This methodology will then be applied to the non-blunted plate in order to verify its accuracy. The base flow results for two blunted plates will then be presented and an analysis of the interaction between the boundary and entropy layers will be given. Finally, conclusions reached from this project will be stated and future work, including the application of this new methodology to the blunted plates, will be laid out.

2 Selected Geometry

There are three total geometries which are studied in this project. Each of these geometries involve a flat plate which has a streamwise length of 200 mm. The first geometry is that of a non-blunted plate, for which the effect of the leading edge is negligible. The other two cases have a blunted leading edge in order to allow for the study of transition reversal. Both of these leading edges are defined by a circle with radii of 0.1 mm and 1 mm, respectively. Each of these leading edges are attached to a flat plate to give a total streamwise length of 200 mm. All streamwise dimensions are measured from the leading edges. Each of the geometries and the above coordinate system is shown in Figure 3.

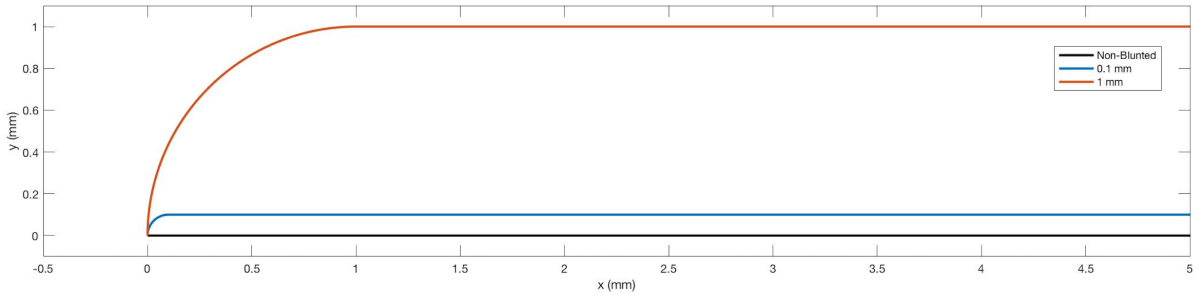

Figure 3: Selected Geometries

Each of the various geometries must be incorporated into a computational domain to allow for the overset of a structured mesh. Each domain is constructed using SolidWorks®. The non-blunted domain and an example of one of the blunted domains (1 mm) are shown in Figures 4 and 5, respectively. For the non-blunted case, the domain is simply that of a rectangle with the bottom boundary acting as the surface of the plate. The height of this rectangle is 60 mm and is determined by estimating the angle of the oblique shock and ensuring the domain is tall enough for the shock to reach the outlet. The domains for the blunted cases are slightly more complex. First, each plate, including the leading edge, is sketched. Next, a quarter-circle is drawn concentric to the quarter-circle which forms the leading edge. The radius of this outer circle is determined once again by estimating the angle of the shock and the height needed for the shock to reach the outlet. A horizontal line is then drawn to connect the bottoms of the two quarter-circles. Finally, a horizontal line is drawn from the top of the outer circle to meet an intersecting vertical line from the end of the plate. With the domains for each geometry constructed, each domain can be overset with a computational grid.

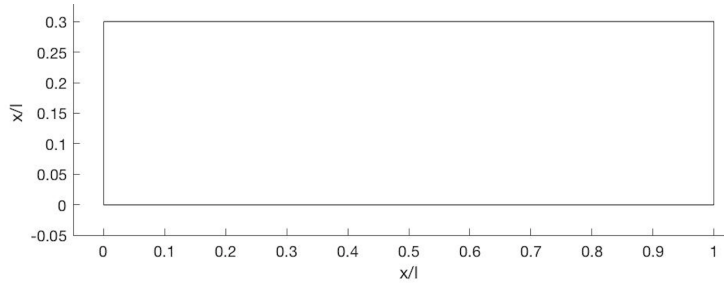

Figure 4: Non-Blunted Plate Domain

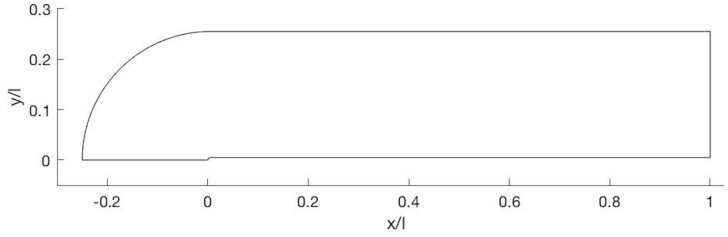

Figure 5: 1mm Blunted Plate Domain

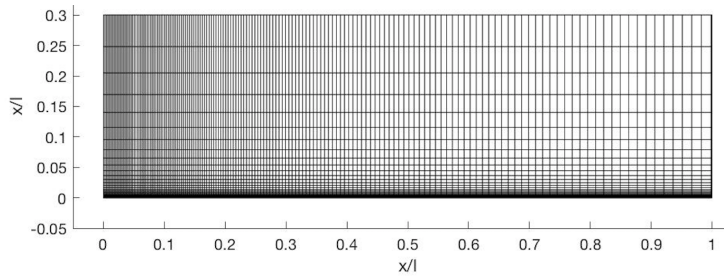

Figure 6: Non-Blunted Plate Grid

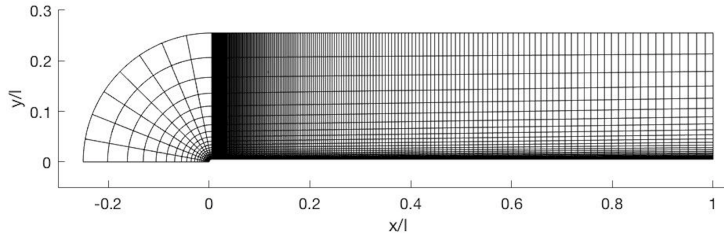

Figure 7: 1mm Blunted Plate Grid

3 Meshing

After determining the geometries of interest for this project, each geometry was meshed in order to allow solution of the flow variables at a discreet set of points. All geometries were meshed in two dimensions using Pointwise® meshing software. Each two-dimensional grid was then manually extruded in the spanwise direction 10 times to obtain the full three-dimensional grid. Finer grid spacings are given in the normal direction closer to the plate as well as in the spanwise direction near the leading edge. These spacings allow for the accurate capture of the main flow features such as the shock, boundary layer, and entropy layer. For consistency, each mesh has defined spacing at the surface of the plate equal to 0.01 mm at the leading edge and 0.02 mm at the end of the domain. This spacing not only provides consistency between the various meshes but also ensures the number of nodes within the boundary layer is approximately the same at all locations in the streamwise direction.

The non-blunted case has a total of 1601 nodes in the streamwise direction, 250 in the normal direction, and 11 in the spanwise direction for a total of approximately 4.4 million nodes. The 0.1

mm blunted case has a total of 2019 nodes in the streamwise direction, 250 in the normal direction, and 11 in the spanwise direction for a total of approximately 5.6 million nodes. Finally, the 1 mm blunted case has 1879 nodes in the streamwise direction, 250 in the normal direction, and 11 in the spanwise direction for a total of approximately 5.2 million nodes. The meshes for the non-blunted case and 1 mm blunted case are shown in Figures 6 and 7, respectively.

4 Solver

The computational solver used in the current project is FDL3DI, a well proven, high-order, Navier-Stokes solver developed by the Air Force Research Laboratory. Convection terms are calculated using a 3^{rd} order Roe scheme, while diffusion terms are calculated using a 6^{th} order compact differencing scheme. Both schemes utilize MUSCL interpolation with a Van Albada flux limiter. Finally, temporal derivatives are calculated using the method of Beam and Warming which is supplemented with Newton-like sub-iterations to provide 2^{nd} order accuracy. More details on the different computational schemes in FDL3DI are given by Gaitonde and Visbal (Gaitonde & Visbal, 1998) (Visbal & Gaitonde, 2002).

All state variables are represented and solved in non-dimensional form such that:

$$u^\star = \frac{u}{u_\infty} \tag{1}$$

$$v^\star = \frac{v}{u_\infty} \tag{2}$$

$$w^\star = \frac{w}{u_\infty} \tag{3}$$

$$\rho^\star = \frac{\rho}{\rho_\infty} \tag{4}$$

$$p^\star = \frac{\rho^\star u^{\star 2}}{\gamma M_\infty^2} \tag{5}$$

where * indicates non-dimensional values. The primary boundary conditions include a freestream Mach number of $M = 6$, a per unit Reynold's number of $Re = 10.5 \times 10^6/m$, and a freestream temperature of 43.8 K. Additionally, the plate is specified as isothermal with $T_w = 293K$. This isothermal temperature is very close to the adiabatic temperature of the wall for the given conditions. Boundary conditions are explicitly defined in FDL3DI and are the same for all three cases

in the current project. Specifically, the inlet condition is defined such that density and streamwise velocity in non-dimensional form are unity, normal velocity and spanwise velocity are both zero, and $p = p_\infty$, such that $p^\star = \frac{1}{\gamma M_\infty^2}$. The boundary condition on the surface of the plate satisfies the no slip condition in all three directions. Additionally, the normal density gradient at the plate surface is zero, and the plate is defined as isothermal. The outlet condition consists of a zero streamwise gradient condition for all state variables and the freestream condition consists of a zero normal gradient for all state variables. Finally, a periodic boundary condition is applied in the spanwise direction. These boundary conditions and the numerical schemes discussed previously are first used to calculate the base flow for the non-blunted plate.

5 Non-Blunted Plate Base Flow Results

For each geometry considered, converged base flow results are obtained from FDL3DI. A brief discussion of these results for the non-blunted plate will be the focus of this chapter. The main features examined in the base flow solutions for each geometry are the shockwaves, generalized inflection points, and boundary layer profiles. For the discussion of the base flows of the two blunted plates, which will be the focus of Chapter 9, a discussion of the entropy layer and it's interaction with the boundary layer will be added to the analysis.

The first feature of interest is the shockwave which can be visualized in multiple ways. Figures 8 and 9 show the mean pressure contours for the flow over the non-blunted plate. These contours are the most basic way to visualize the oblique shock and the angle at which it is forming. From the contours, the shockwave is estimated to have an angle of approximately 10^o. The lower limit for the shock angle is the Mach angle $\mu = sin^{-1}(1/M)$. For this Mach 6 flow, that gives a Mach

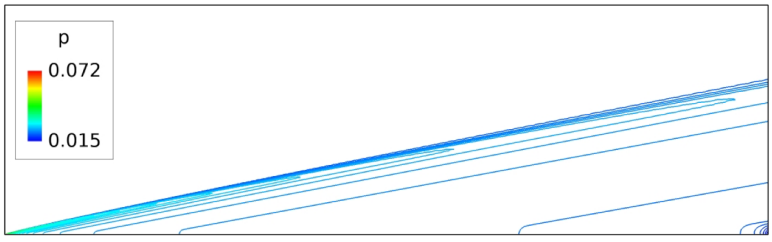

Figure 8: Non-Blunted Plate Base Flow Pressure Contour

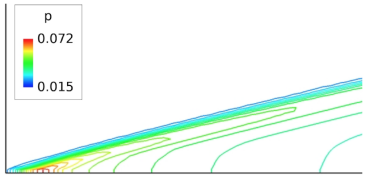

Figure 9: Non-Blunted Plate Base Flow Pressure Contours (Leading Edge)

angle of approximately 9.6^o, which demonstrates that the shockwave in this flow is very near the weak limit of a Mach wave.

The shockwave can also be visualized by plotting the generalized inflection point (GIP). The GIP provides significant insight into several of the main flow features studied here. The GIP is defined as $\rho\frac{\delta u}{\delta y}$ and is plotted for five different locations on the non-blunted plate in Figure 10. The inflection at the highest y location in each plot is a result of the gradients in the region of the shockwave. This inflection is thus used to determine the height of the shockwave at each x location which is represented by a red dashed line. The increase in the height of the shock with increasing distance from the leading edge is seen to be perfectly linear as one would expect for an oblique shock on a non-blunted plate. The angle of the oblique shock is calculated as 9.93^o. Furthermore, it can be seen that the magnitude of this inflection decreases at each x location, demonstrating the weakening of the shockwave further downstream.

The other inflection point seen in each plot of Figure 10 is much closer to the surface of the plate and is a result of the boundary layer. This inflection can be better seen in Figure 11, which is the same GIP plot scaled to show the boundary layer region. Unlike the inflection point for the shockwave, the height of the boundary layer inflection point does not increase linearly with distance from the leading edge but scales with the boundary layer thickness. The height of the boundary layer at each location is also determined and plotted in Figures 10 and 11. In order to determine the boundary layer height, the location of the shock is first determined from the GIP as discussed previously. The boundary layer thickness is then defined as the height where the streamwise velocity equals 99% of the streamwise velocity just below the shockwave.

The boundary layer heights calculated as outlined above are also shown in Figure 12 which plots the non-dimensional velocity and temperature profiles in the boundary layer region for the same five locations. Also plotted is the self-similar boundary layer velocity and temperature profiles obtained using the Howarth-Dorodnitsyn transformation (Dorodnitsyn, 1942). Comparing the numerical solution with the self-similar profiles provides a final validation of the accuracy of the base flow solution before adding perturbations to the flow.

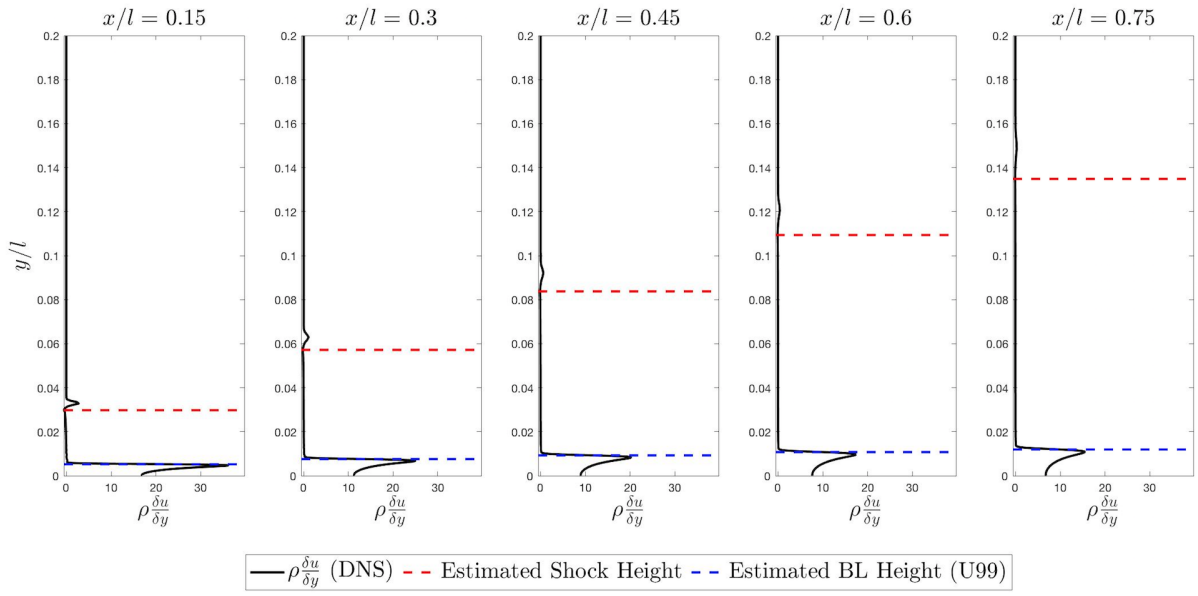

Figure 10: Non-Blunted Plate Full Generalized Inflection Point

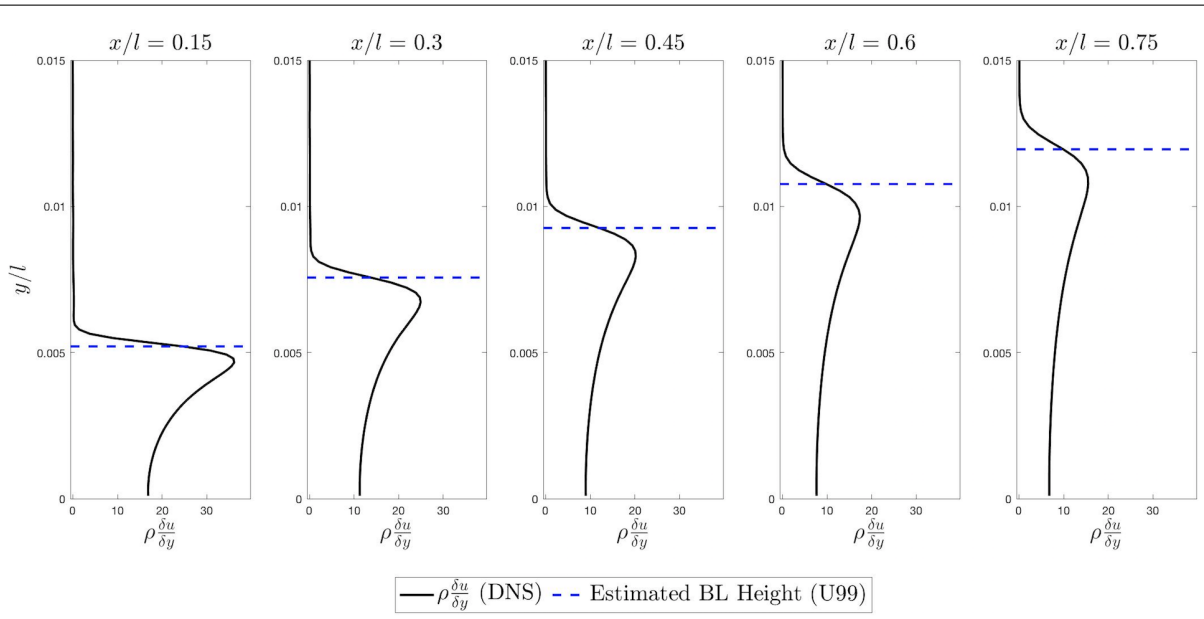

Figure 11: Non-Blunted Plate Boundary Layer Generalized Inflection Point

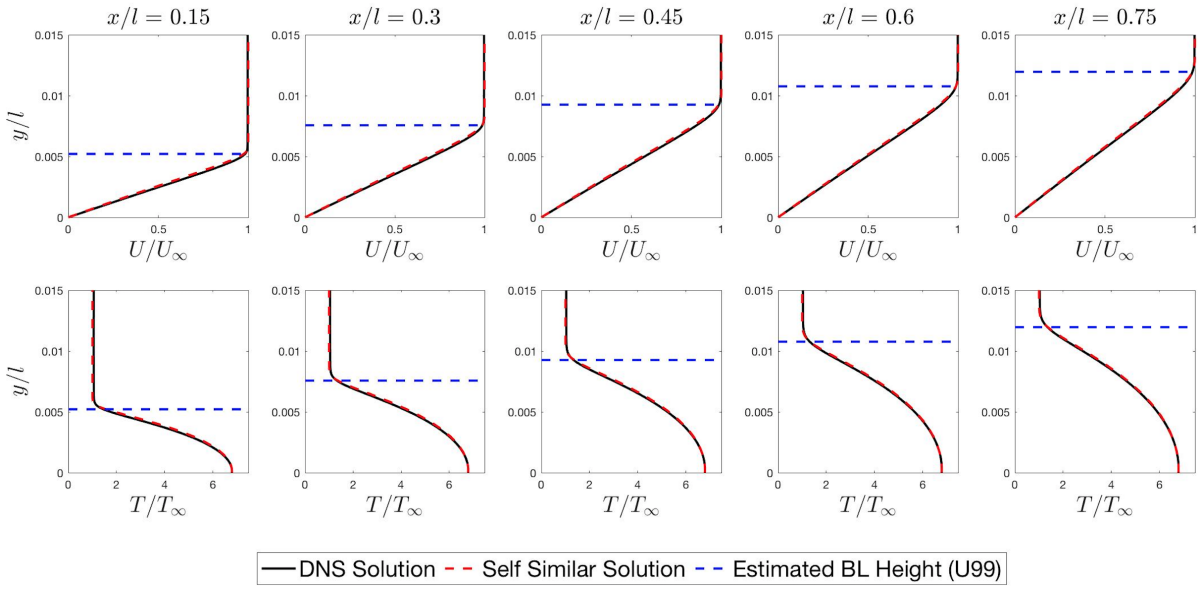

Figure 12: Non-Blunted Plate Boundary Layer Profiles

6 Linear Stability Theory Results

A temporal LST analysis is now performed on the base flow results for the non-blunted plate at $x/l = 0.75$. For simplicity, this analysis is performed on the self-similar profile at the relevant conditions. As seen in the previous chapter, the DNS results match perfectly with the self-similar profile and thus analyzing this profile will provide the same results as analyzing the DNS itself.

The full phase speed plot is shown in Figure 13 for $\alpha = 0.1$ and phase speed $c = \omega/\alpha$. Most of the visible modes are spurious modes that result from the grid spacing of the LST analysis and don't represent the actual physics of the flow. Figure 14 shows the same phase speed plot for phase speeds close to that of the disturbances which travel at $c = 1$. Spurious modes are detected by varying the grid spacing and streamwise wavenumber, as different spurious modes appear for different conditions. The entropic and vortical continuous modes are shown as a vertical branch at $c = 1$. Additionally, the slow and fast continuous acoustic modes are also shown in Figure 14. The first slow and fast continuous acoustic mode are seen to have phase speeds of $c = 1 - 1/M$ and $c = 1 + 1/M$, respectively. Finally, the two discreet s and f modes are shown, which converge to the same phase speeds of $c = 1 - 1/M$ and $c = 1 + 1/M$, respectively for increasing streamwise wavenumber.

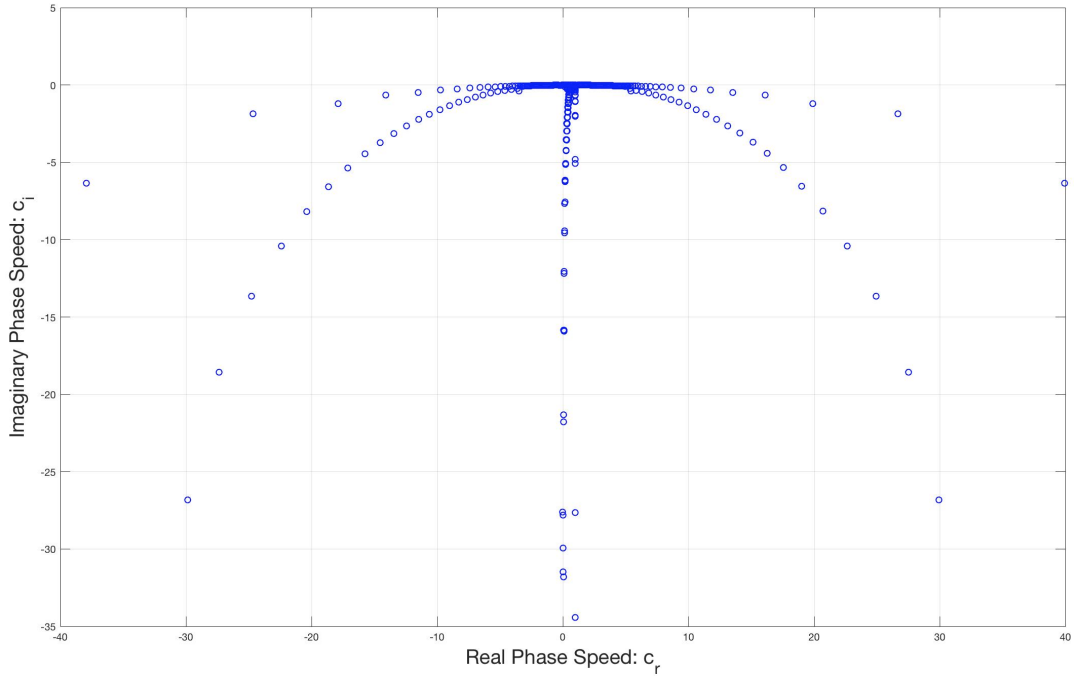

Figure 13: Non-Blunted Plate Full Eigenspectrum

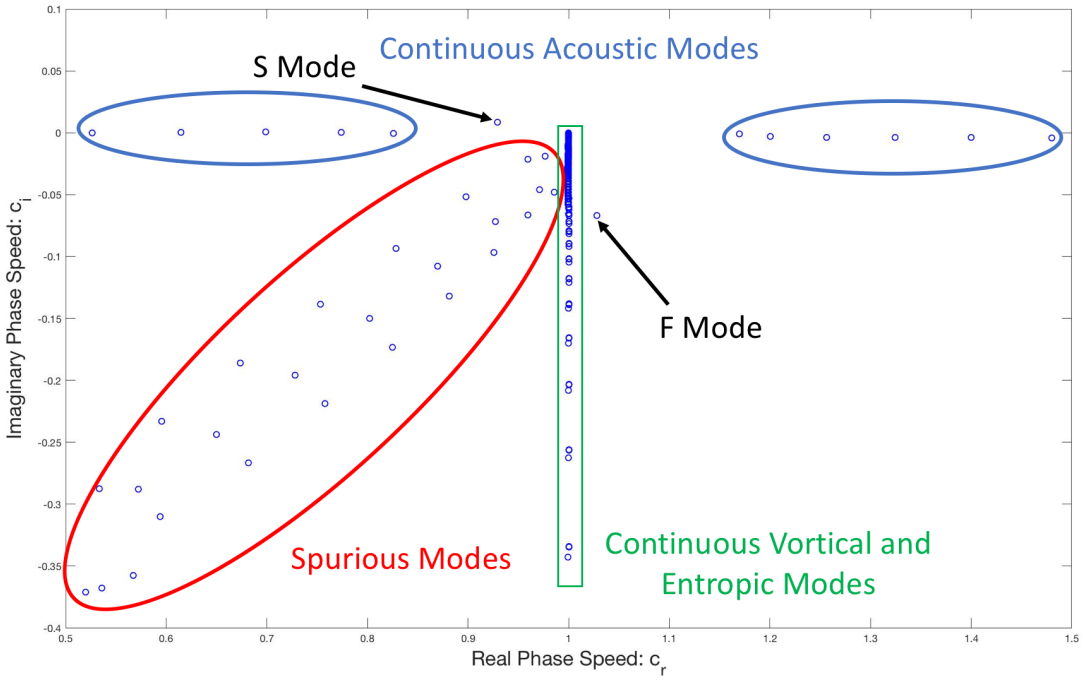

Figure 14: Non-Blunted Plate Modes

In addition to the temporal LST results discussed above, spectral LST results often used by Fedorov will be used for validation of the non-blunted plate unstable frequency in later chapters. Specifically, Fedorov has determined for the non-blunted geometry at Mach 6, the most unstable frequency is $F = 35.1$ at $x/l = 0.75$ (Egorov, Sudakov, & Fedorov, 2006).

7 Approach to Extracting Most Unstable Frequency

As was demonstrated in the previous chapter, for a non-blunted plate the most unstable frequency at any location can be determined from LST. This is not the case, however, for blunted objects. Therefore, with a goal of studying several blunted plates, it is necessary to develop an alternative method for determining the most unstable frequency at any given location. This chapter will describe such a method developed in this project. This method involves studying the receptivity of the flow to several types of random forcing. In addition to three types of random forcing, one single frequency forcing case will be studied to use as a baseline to which the random forcing cases can be compared. Each of these forcing techniques will be applied to the non-blunted plate in Chapter 8 in order to validate this method.

The first forcing technique to be utilized is a single frequency forcing. This technique will be referred to as Case 1. Specifically, the single frequency to be forced is the frequency determined by LST in Chapter 6 to be the most unstable at $x/l = 0.75$, $F = 35.1$. The flow will be forced at this frequency using a wall-normal velocity forcing at the surface of the plate within the range $0.05 \leq x/l \leq 0.075$. The forcing is defined as:

$$v = Af(x)sin(2\pi Ft) \tag{6}$$

where v is the wall normal velocity applied at each location on the surface, $A = 1 \times 10^{-3}$ is the amplitude of the perturbation, and $F = 35.1$ is the most unstable frequency as determined by LST for $x/l = 0.75$.

The three random forcing techniques applied all follow the same general approach. The random forcing techniques are random freestream velocity perturbations, random freestream pressure perturbations, and a random wall-normal blowing-suction section for the same range of x locations as Case 1. These techniques will be referred to as Cases 2, 3, and 4, respectively. The forcing

functions for each of these cases are of the same form such that:

$$q = q_0 + A(2r - 1) \tag{7}$$

where q is a general variable to which the forcing is applied, q_0 is the general variable's base flow value, $A = 1 \times 10^{-3}$ is the amplitude of the disturbance, and $0 \leq r \leq 1$ is a random number. This forcing function ensures that the average perturbation is zero, such that the mean flow is unchanged. The specific forcing functions used for Cases 2, 3, and 4 are shown in equations 8, 9, and 10, respectively.

$$u = u_\infty + A(2r - 1) \tag{8}$$

$$p = p_\infty + A(2r - 1) \tag{9}$$

$$v = v + A(2r - 1) = A(2r - 1) \tag{10}$$

Results from each of these random forcing techniques, as well as the single frequency forcing, applied to the non-blunted plate are analyzed in Chapter 8. The results from each of these cases are studied in the same manner, primarily utilizing two tools. First, a chronogram is created which allows the evolution of the pressure fluctuations in time and space to be studied. Second, a temporal FFT of the pressure fluctuations is performed at each location on the surface of the plate using Welch's method (Welch, 1967). The FFT at each location will allow the frequency with the largest amplitude, and thus the most unstable frequency, at each location to be extracted.

8 Validation

The methodology laid out in Chapter 7 is now applied to the base flow for the non-blunted plate and the results from each forcing technique are compared to the results obtained from LST in Chapter 6. The amplitude of the pressure fluctuations resulting from the forcing in Case 1 are shown in the chronogram in Figure 15. It can be seen that the pressure disturbances are initially small but grow as they move downstream and eventually reach a maximum around $x/l = 0.75$. This result matches with the result from LST since the single frequency being forced was determined to have a max growth rate at $x/l = 0.75$. Next, an FFT is performed on the pressure fluctuations at four different locations on the surface and these results are shown in Figure 16. From Figure 16 it

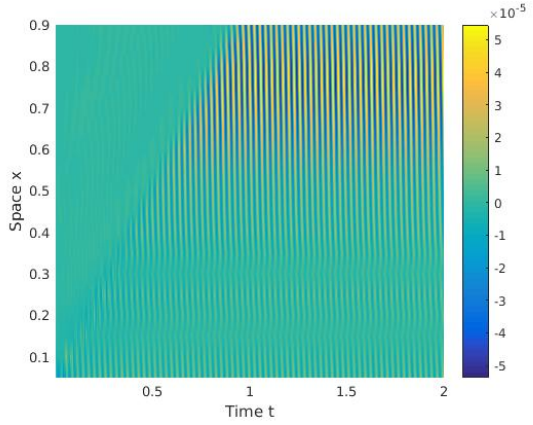

Figure 15: Non-Blunted Plate Case 1: Chronogram

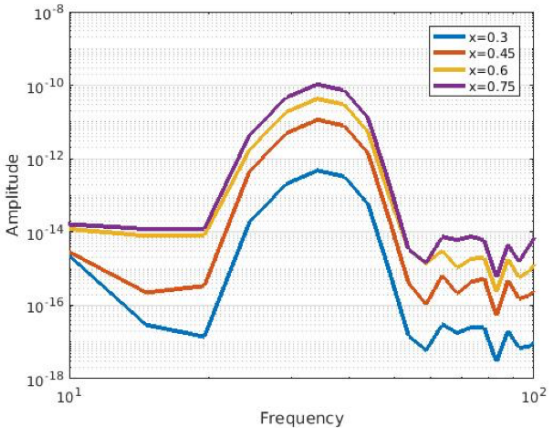

Figure 16: Non-Blunted Plate Case 1: FFT (Select Locations)

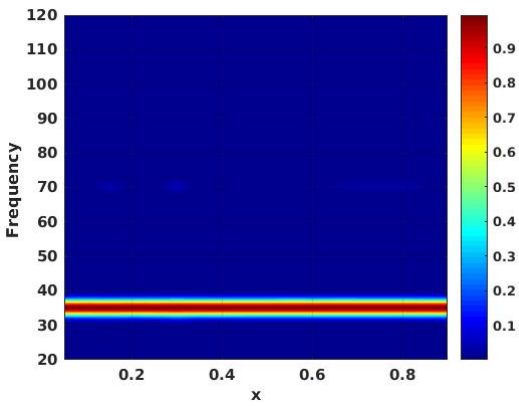

Figure 17: Non-Blunted Plate Case 1: FFT (All Locations)

is seen that the most amplified frequency at each location is the same. This fact is further demonstrated in Figure 17 which shows the same FFT performed for every location on the surface of the plate. Furthermore, the most amplified frequency at each location is simply the frequency which the flow is forced at. The FFT at each location extracts the most unstable frequency as $F = 34.18$, a 2.6% error from the forced frequency, $F = 35.1$. This small error can be attributed to the method in which the FFT itself is calculated. Obviously, extracting the most unstable frequency by forcing the flow at the predetermined most unstable frequency is a trivial result. Therefore, the results of Case 1 are treated as simply a baseline to which results from the other cases are compared.

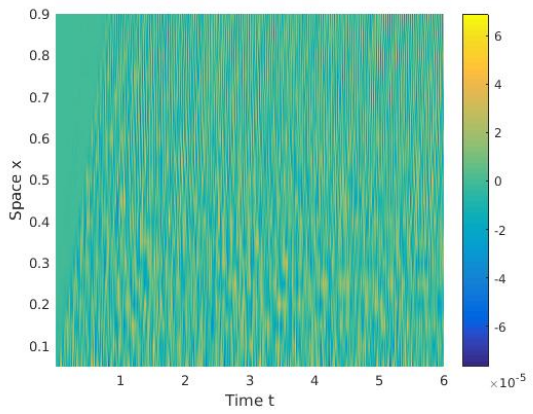

Figure 18: Non-Blunted Plate Case 2: Chronogram

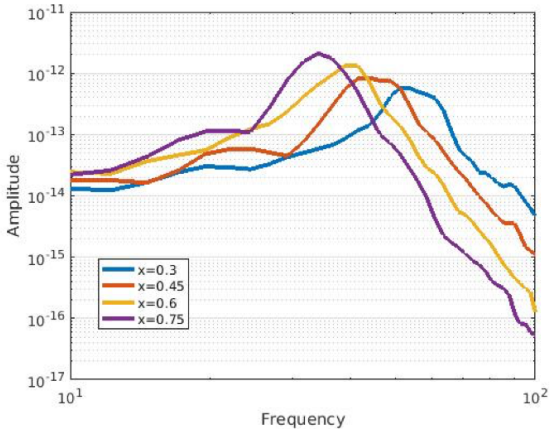

Figure 19: Non-Blunted Plate Case 2: FFT (Select Locations)

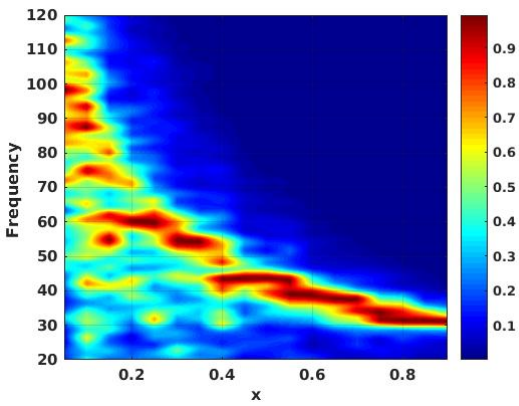

Figure 20: Non-Blunted Plate Case 2: FFT (All Locations)

Once again, Case 2 involves the forcing of the flow with random freestream velocity disturbances. The chronogram for Case 2 is shown in Figure 18. Unlike the chronogram for Case 1, Figure 18 doesn't show any clear regions where the pressure fluctuations are amplified. Not only is there no obvious spatial pattern, but the amplitude at each location now changes with time as the flow is now being randomly forced continuously. An FFT is again performed at the same four locations on the surface and the results are shown in Figure 19. Unlike for the previous case of single frequency forcing, in Figure 19, the most amplified frequency is different at each location. Since no frequency is specified, the most amplified frequency at each location is associated with the boundary layer

thickness at each location. Yet, looking at the FFT for $x/l = 0.75$, the most unstable frequency is calculated as $F = 34.18$, the same value obtained from single frequency forcing. The relationship between streamwise location and unstable frequency is further demonstrated in Figure 20, where the FFT is plotted for all locations. From the FFT it can be seen that close to the leading edge essentially all frequencies are amplified, demonstrating that the flow is now being randomly forced in the freestream. However, as the disturbances convect downstream, it is seen that higher frequency disturbances are damped out. A strong correlation emerges between the distance from the leading edge and the most amplified frequency. The most unstable frequency at a given location decreases for locations farther downstream, meaning high frequency disturbances are needed to make the boundary layer unstable close to the leading edge. This correlation is not linear but related to the boundary layer thickness at each location. Most importantly, the results of the FFT extract the most unstable frequency at $x/l = 0.75$ as $F = 34.18$, the exact same value obtained from the single frequency forcing.

The analysis is next repeated for Case 3, random freestream pressure forcing. The chronogram for Case 3 is shown in Figure 21. Comparing Figure 21 with Figure 18 from Case 2, it is clear the two cases result in similarly random pressure fluctuations and no noticeable differences are seen. An FFT is first performed at the same four locations, the results of which are shown in Figure 19. Again, the most amplified frequency at each location is different and the same trend is seen between this frequency and the streamwise location. Looking specifically at $x/l = 0.75$, the most unstable frequency extracted by the FFT is exactly the same as was obtained from Cases 1 and 2: $F = 34.18$. This demonstrates that not only can these unstable frequencies be extracted by applying random forcing, but that the frequencies are independent of the manner in which the random forcing is applied. One noteworthy difference between Cases 2 and 3 is that the amplitudes in Case 3 are approximately an order of magnitude greater than the amplitudes measured in Case 2. This suggests that this particular flow is more receptive to freestream pressure disturbances than freestream velocity disturbances. Finally, the results of the FFT at all locations on the plate are presented in Figure 23. Comparing Figures 20 and 23, reveals no significant differences. Once again it is seen that the most unstable frequency decreases with increasing streamwise location.

This analysis is repeated one final time for the random wall-normal blowing-suction section in Case 4. The resulting chronogram is shown in Figure 24. Again, no significant differences

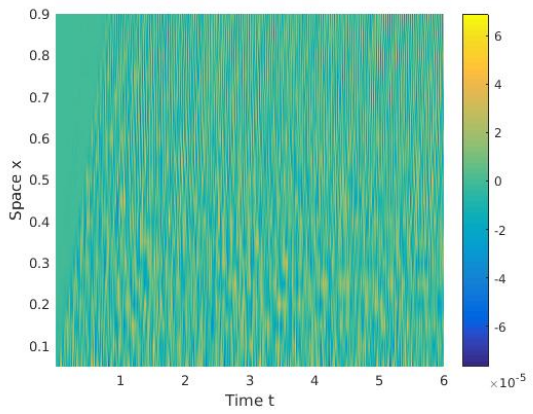

Figure 21: Non-Blunted Plate Case 3: Chronogram

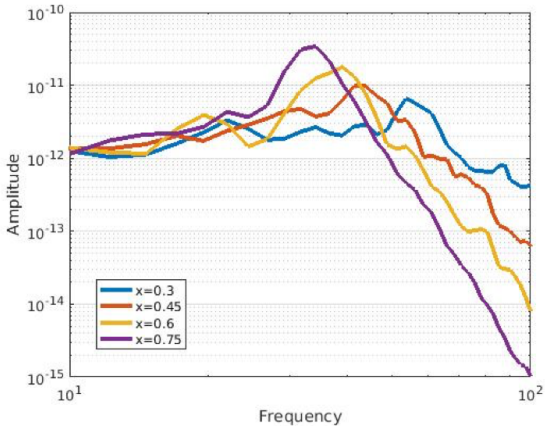

Figure 22: Non-Blunted Plate Case 3: FFT (Select Locations)

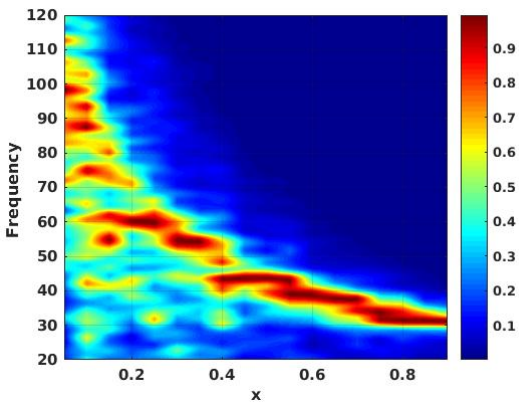

Figure 23: Non-Blunted Plate Case 3: FFT (All Locations)

are seen by comparing this result to those of Cases 2 and 3. Figure 25 again shows the FFT results at four locations on the surface. The most unstable frequency is once again calculated as $F = 34.18$ for $x/l = 0.75$. However, the amplitudes for this case were approximately an order of magnitude less than those from random freestream velocity disturbances and approximately two orders of magnitude less than those from random freestream pressure disturbances. As a result, it is determined that this flow is less receptive to random wall-normal velocity disturbances than either random pressure or velocity disturbances in the freestream. Finally, the FFT for all locations is presented in Figure 26 which is seen to be almost identical to the same plot for Cases 2 and 3.

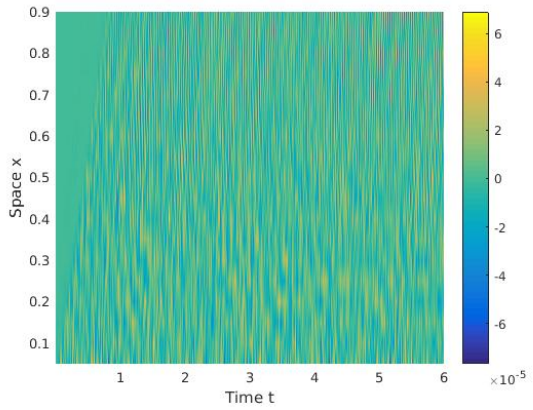

Figure 24: Non-Blunted Plate Case 4: Chronogram

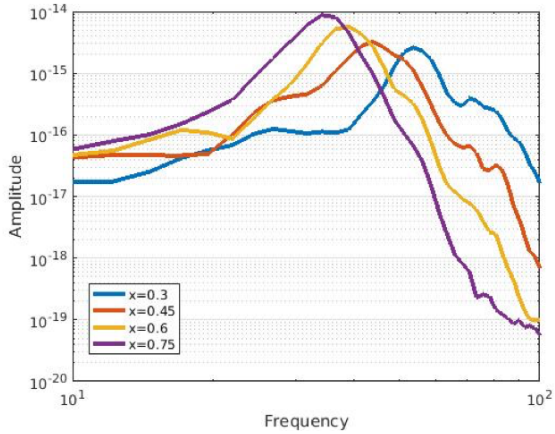

Figure 25: Non-Blunted Plate Case 4: FFT (Select Locations)

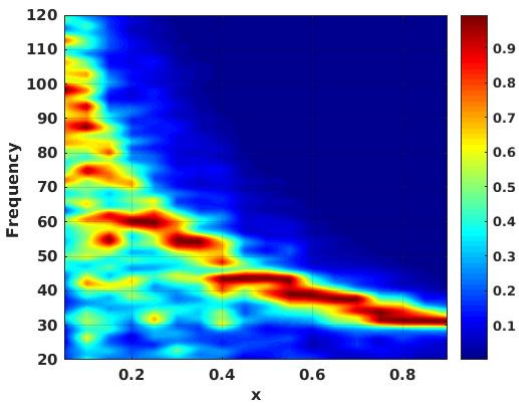

Figure 26: Non-Blunted Plate Case 4: FFT (All Locations)

Having found the most unstable frequency from the DNS, regardless of forcing technique, at $x/l = 0.75$ to be $F = 34.18$, disturbances are now added to the base flow by forcing the flow at $F = 34.18$. After the flow is allowed to convect downstream, the pressure fluctuation at each point on the surface is calculated and plotted in Figure 27. When just this single frequency is forced, it is seen that the location where the disturbance is most amplified is approximately $x/l = 0.8$. This represents a 6% error from $x/l = 0.75$, the location where the previous FFT analyses determined $F = 34.18$ as the most unstable frequency.

The same can be done for any frequency to determine the location of it's max growth rate.

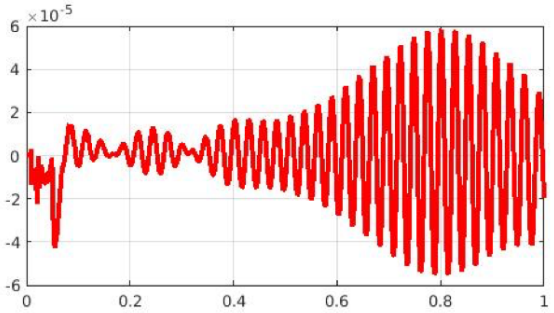

Figure 27: Non-Blunted Plate Surface Pressure Fluctuations ($F = 34.18$)

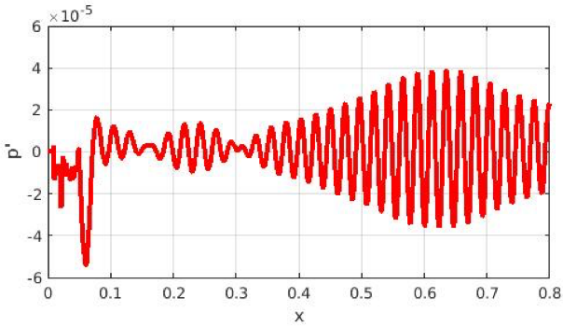

Figure 28: Non-Blunted Plate Surface Pressure Fluctuations ($F = 39.06$)

For example, although not discussed previously, the FFT results from each of the random forcing techniques also determined the most unstable frequency at $x/l = 0.6$ to be $F = 39.06$. This single frequency is forced and the pressure fluctuations at the wall are plotted in Figure 28. Here it is seen that this frequency is most amplified at approximately $x/l = 0.625$, about a 4% error from $x/l = 0.6$ where the FFT determined this frequency to be the most unstable.

To summarize, by applying various random forcing techniques to the base flow of the non-blunted plate and performing an FFT of the pressure fluctuations, the most unstable frequency at any location can be determined. This method does not involve using LST but is able to match the results from LST with great accuracy. Additionally, this approach is able to provide these unstable frequencies regardless of the manner in which the random forcing is applied. Furthermore, a clear correlation is observed between the distance from the leading edge and the most unstable frequency at that location. It is also seen that the flow for the non-blunted plate is most receptive to random freestream pressure disturbances and least receptive to random wall-normal velocity disturbances. Finally, the location of max growth rate for any of the unstable frequencies determined by the FFT can be confirmed by forcing the flow at the given frequency and determining the location of max pressure fluctuations on the surface. The demonstration of the ability to extract unstable frequencies, as well as the locations where they are most amplified, without LST solves one of the major challenges in studying transition reversal by providing a viable method for determining these frequencies for blunted geometries.

9 Blunt Cases Base Flow Results

While the application of the approach discussed in the previous chapter to the blunted plates will be the subject of future writing, a brief discussion of the base flow results is presented here. The base flow results for the blunted plates are analyzed in the same manner as the non-blunted plate in Chapter 5. Of course, the entropy layer which only exists over the blunted plates is also analyzed here.

The mean pressure contours are shown for the full 0.1mm and 1mm blunted plate domains in Figures 29 and 30, respectively. Additionally, pressure contours for just the leading edge regions are shown in Figures 31 and 32. While difficult to see, there is a noticeable difference in the shock angle for the two geometries. The shock angle for the 1mm blunted plate is slightly larger than that of the 0.1mm plate. This difference can probably best be seen by examining the height at which the pressure contour leaves each domain. The stronger bow shock and larger stand-off distance, however, are easily seen on the 1mm plate when comparing the leading edge regions. Another visualization of the shock for each geometry is provided by examining the GIP.

Figure 33 shows the generalized inflection point for the 0.1 mm blunted plate at the same five locations which were analyzed for the non-blunted plate. Additionally, the GIP is also plotted for the boundary and entropy layer region in Figure 34. The same plots are shown for the 1mm blunted plate in Figures 35 and 36. The shock height is determined in the same manner as was done for the non-blunted plate and is again sketched on each plot. Unlike the non-blunted plate where the shock height increased perfectly linearly with increasing x position, the shock height for the 0.1 mm plate shows some small curvature of the bow shock. The shock height of the 1mm plate reflects a significantly stronger curvature due to a larger bow shock. The boundary layer height for each geometry is again approximated by finding the height where the streamwise velocity reaches 99% of the velocity just below the shock. The entropy layer height is also approximated in an equivalent manner. Both the boundary layer and entropy layer are seen to be significantly thicker for the 1mm plate than the 0.1mm plate. In Figure 34, another inflection point begins to become visible which is an inflection point within the entropy layer. Due to the small bluntness of the 0.1mm plate, this inflection is difficult to see but it can be seen much more clearly for the 1mm blunted plate in Figure 36. This entropy layer inflection point can be seen at a height of approximately $y/l = 0.01$ in the first plot of Figure 36. This inflection point appears to diminish significantly as the flow

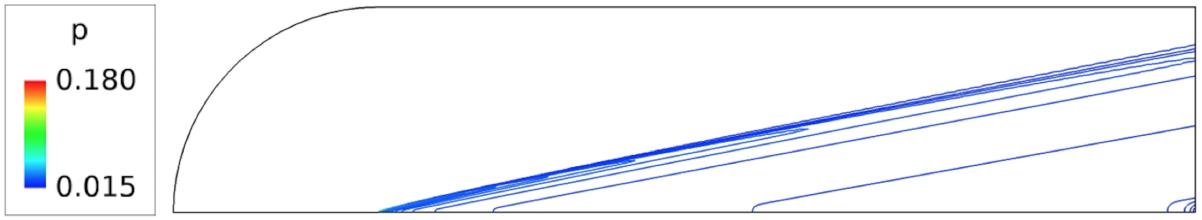

Figure 29: 0.1mm Blunted Plate Base Flow Pressure Contour

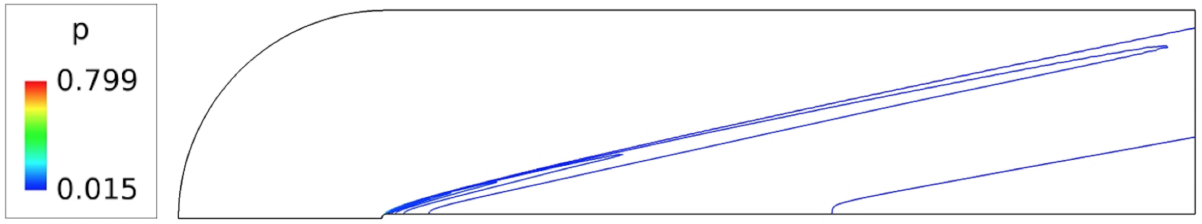

Figure 30: 1mm Blunted Plate Base Flow Pressure Contour

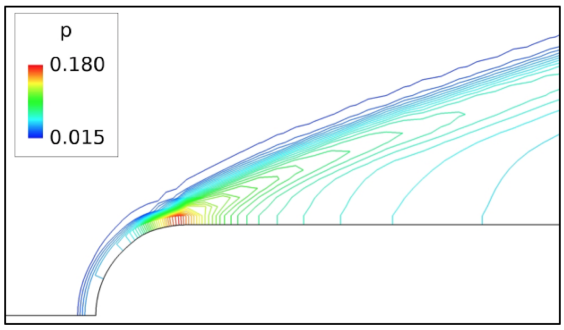

Figure 31: 0.1mm Blunted Plate Base Flow Pressure Contours (Leading Edge)

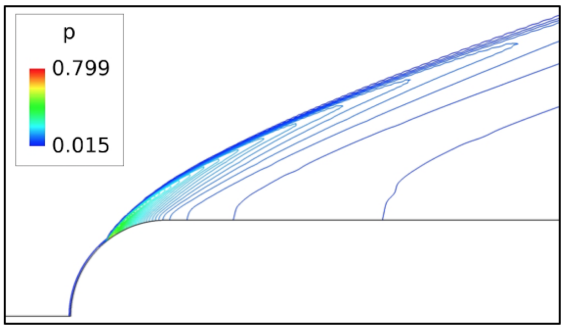

Figure 32: 1mm Blunted Plate Base Flow Pressure Contours (Leading Edge)

moves downstream. Finally, the non-dimensional boundary layer velocity and temperature profiles are plotted in Figures 37 and 38 for the 0.1mm and 1mm blunted plates, respectively.

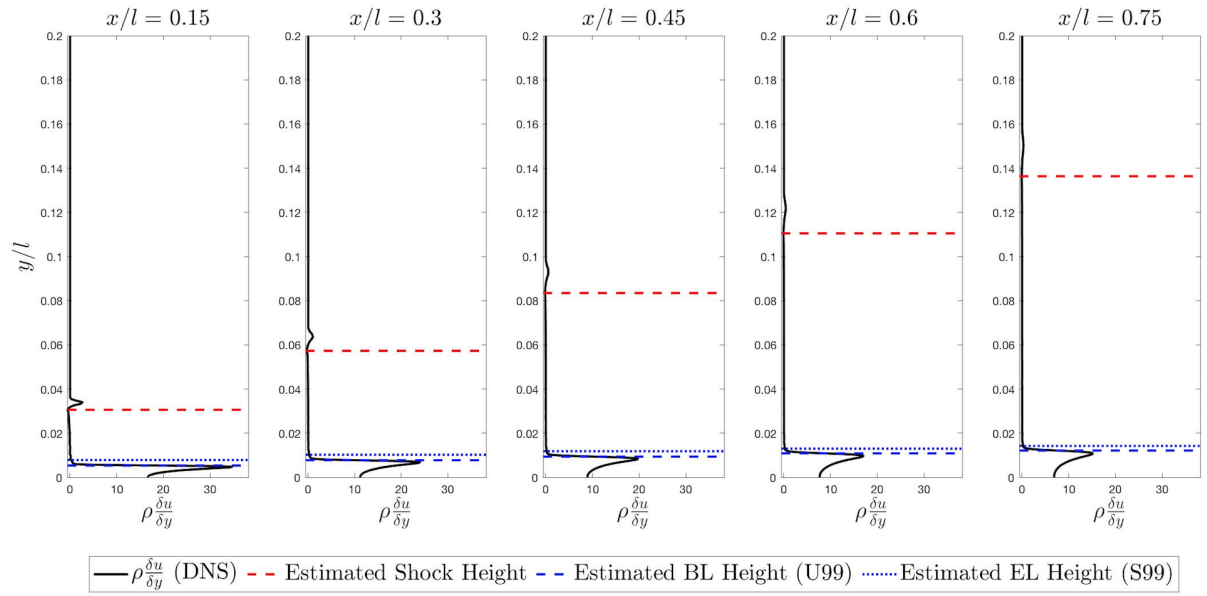

Figure 33: 0.1mm Blunted Plate Full Generalized Inflection Point

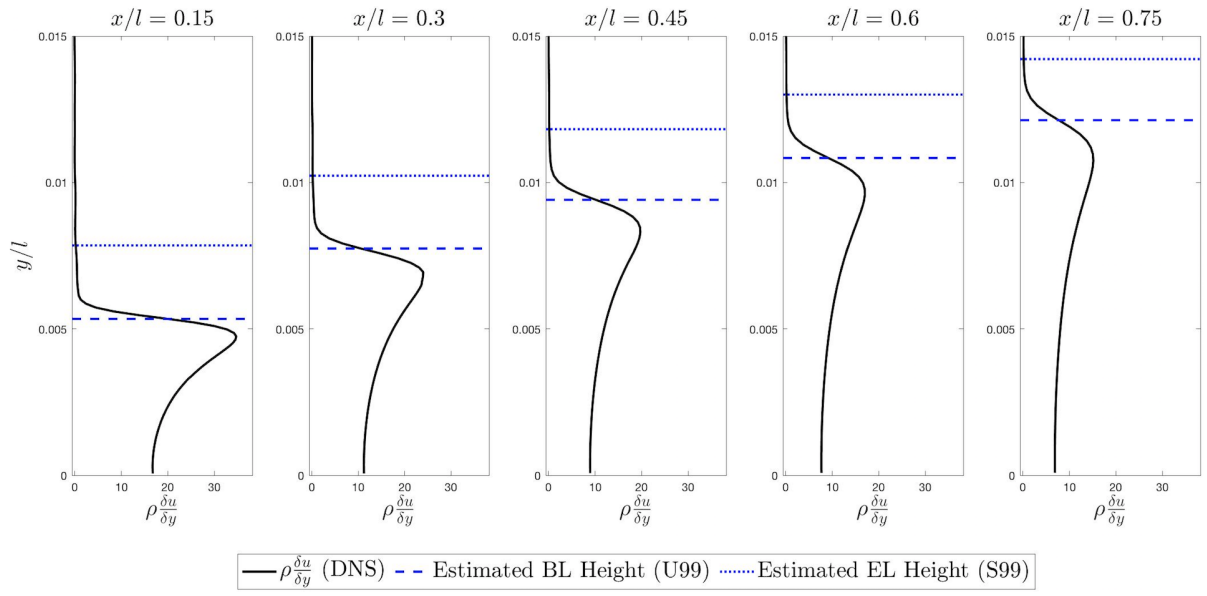

Figure 34: 0.1mm Blunted Plate Boundary Layer Generalized Inflection Point

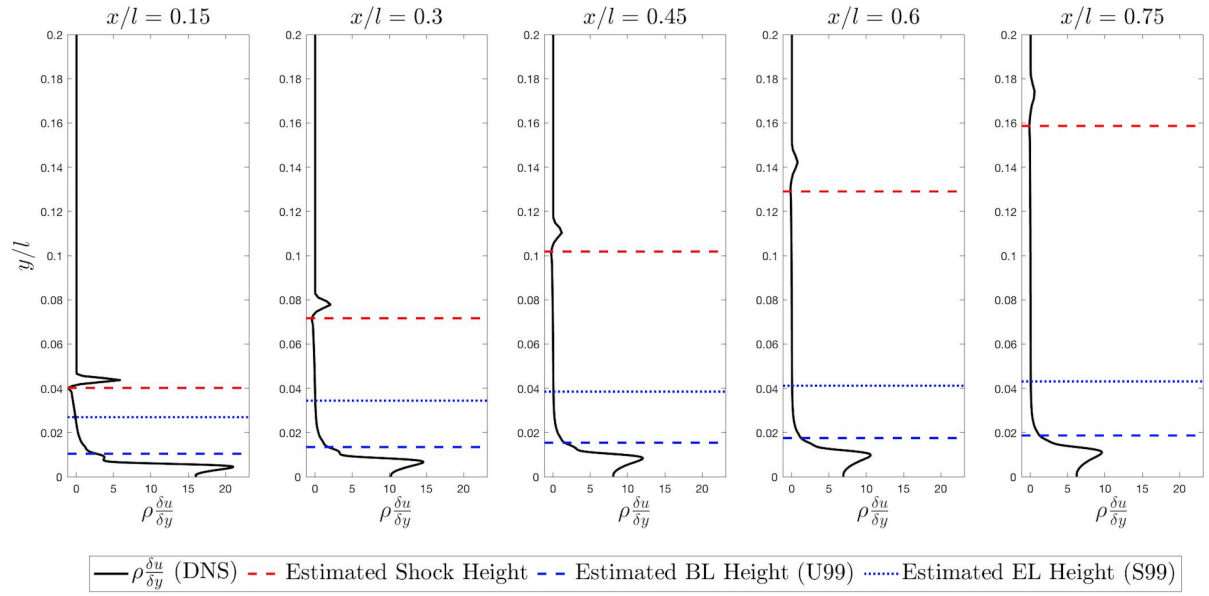

Figure 35: 1mm Blunted Plate Full Generalized Inflection Point

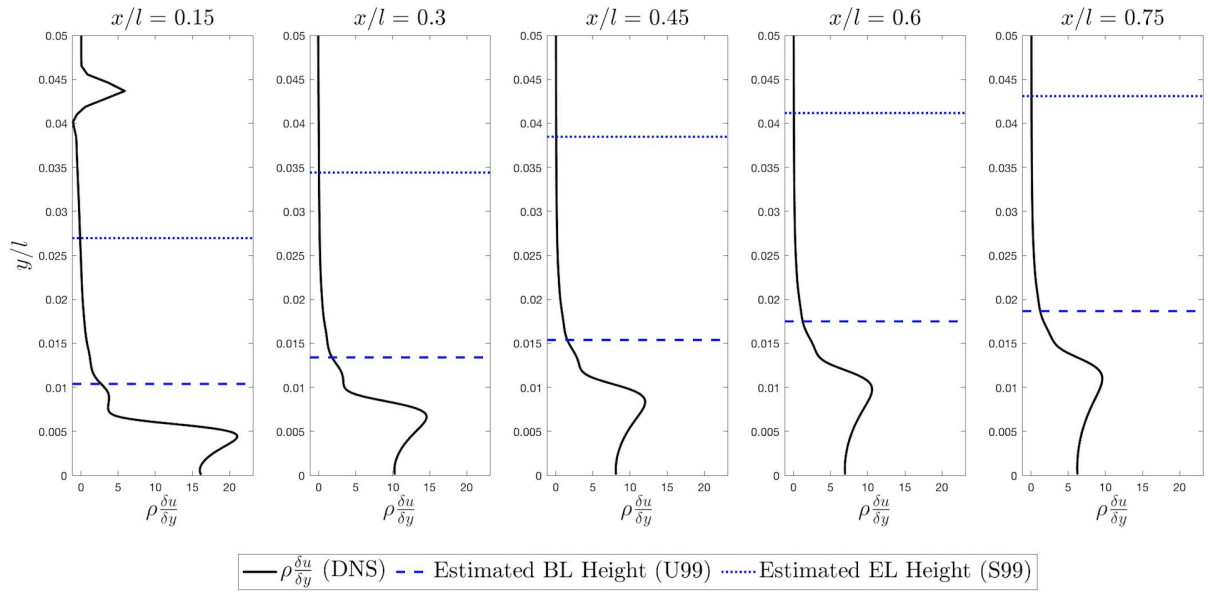

Figure 36: 1mm Blunted Plate Boundary Layer Generalized Inflection Point

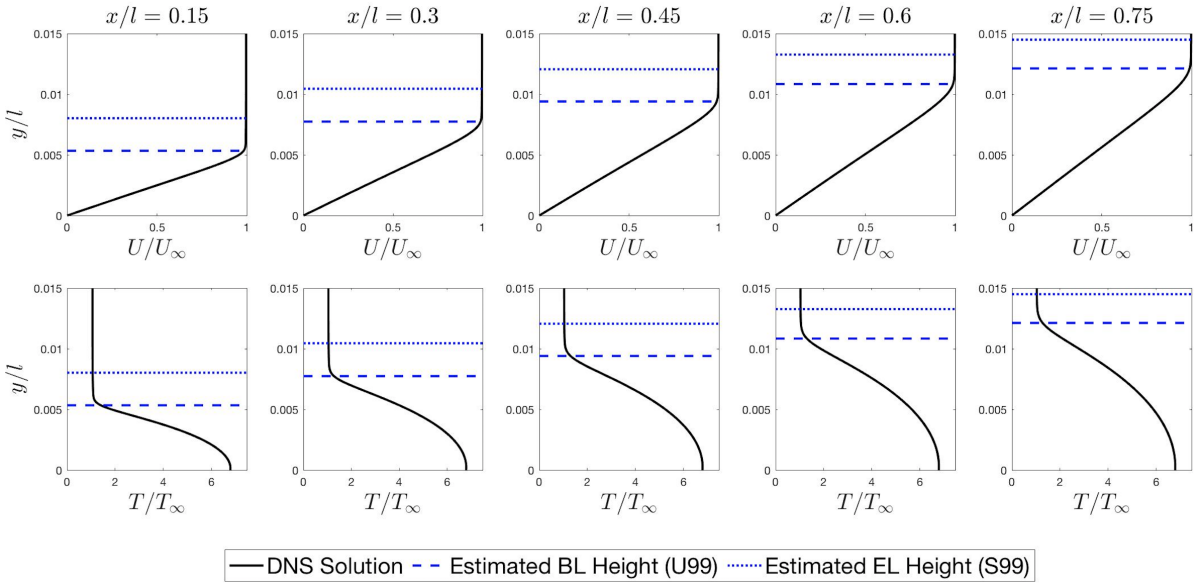

Figure 37: 0.1mm Blunted Plate Boundary Layer Profiles

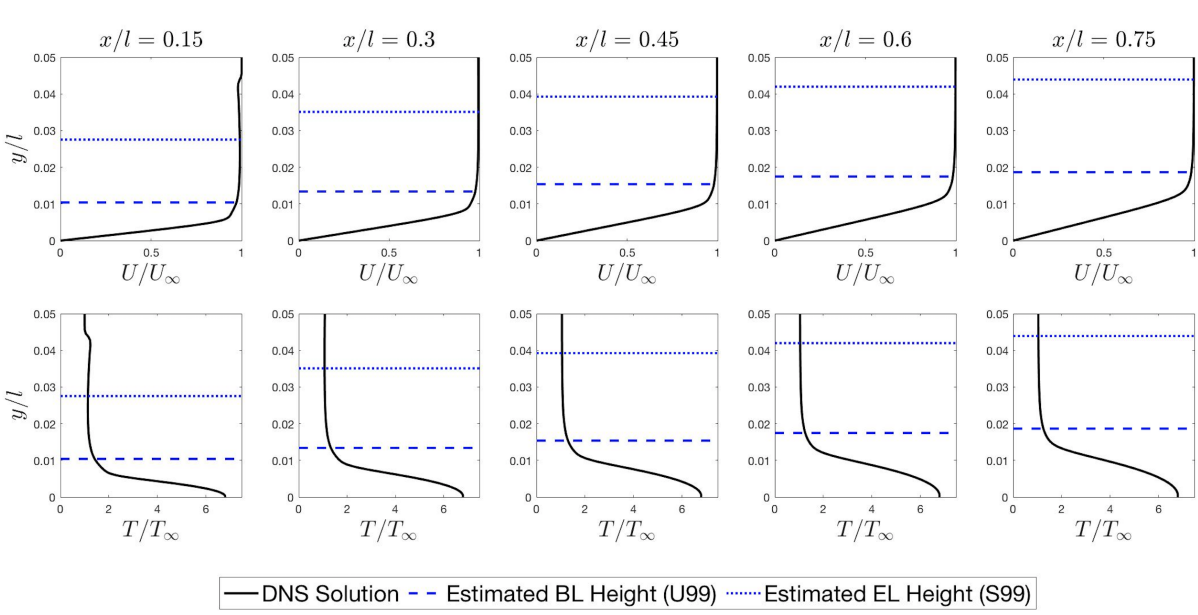

Figure 38: 1mm Blunted Plate Boundary Layer Profiles

The interaction between the boundary and entropy layers is an important feature of flow over blunted objects which must be better understood as part of the study of reversal. The diminishing of the inflection point within the entropy layer seen in Figure 36 as the flow moves downstream is a possible indicator of the swallowing of the entropy layer. Swallowing happens when the height of the entropy layer stops increasing and the boundary and entropy layers reach the same thickness. However, from the estimations of the heights of the boundary and entropy layers, it does not appear that the domain is long enough for the entropy layer to be swallowed. The distance between the boundary and entropy layers for each blunted plate first increases near the leading edge and then begins to decrease. Therefore, it is likely that by extending the domain farther downstream, the estimation of the boundary and entropy layer heights would show the swallowing of the entropy layer. Since these height estimations and the diminishing of the entropy layer inflection point can't be reconciled, it can not be concluded whether the entropy layer of either blunted plate is swallowed within the current domain.

10 Conclusions and Future Work

The conclusions reached as part of this project are summarized as follows:

- Base flow results were obtained and analyzed for both the non-blunted and the 0.1mm and 1mm blunted plates.
- The shock, generalized inflection point, boundary layer, and entropy layer were compared for each geometry.
- The generalized inflection point and the estimated heights of the boundary and entropy layers provided contradicting conclusions about whether or not the entropy layer is swallowed within the domain studied.
- A new methodology based on random forcing was developed which allows for the most unstable frequency at a given location in a flow to be determined without LST.
- This methodology was validated on a non-blunted plate and compared to the results of LST to ensure it's accuracy.

- Finally, this methodology provides results that are independent of the manner in which the flow is randomly forced and depends only on the geometry and flow conditions.

Ongoing and future work related to this project includes the following:

- Application to the blunted plates whose base flows were discussed here of the methodology developed to extract unstable frequencies at any location.
- An expansion of the blunted plates being studied to also include plates with leading edge radii of 0.05, 0.5, and 5mm.
- Attempting to observe transition reversal by analyzing the unstable frequencies at various locations on each blunted geometry.
- Using Doak's Decomposition to analyze the fluid-thermodynamic components of the perturbed flows to determine which components are significant in the blunted cases.

References

Batt, R., & Legner, H. (1983). A review of roughness-induced nosetip transition. *AIAA Journal*, *21*(1), 7–22.

Brinich, P. F. (1956). Effect of leading-edge geometry on boundary-layer transition at mach 3.1.

Brinich, P. F., & Sands, N. (1957). Effect of bluntness on transition for a cone and a hollow cylinder at mach 3.1.

Cook, D. A., Thome, J., Brock, J. M., Nichols, J. W., & Candler, G. V. (2018). Understanding effects of nose-cone bluntness on hypersonic boundary layer transition using input-output analysis. In *2018 aiaa aerospace sciences meeting* (p. 0378).

Dorodnitsyn, A. (1942). Boundary layer in a compressible gas. *Prikl. Mat. Mekh*, *6*(6), 449–486.

D'yakov, S. (1958). The interaction of shock waves with small perturbations. i. *Soviet Phys. JETP*, *6*.

Egorov, I., Sudakov, V., & Fedorov, A. (2006). Numerical modeling of the receptivity of a supersonic boundary layer to acoustic disturbances. *Fluid Dynamics*, *41*(1), 37.

Gaitonde, D. V., & Visbal, M. R. (1998). *High-order schemes for navier-stokes equations: algorithm and implementation into fdl3di* (Tech. Rep.). Air Force Research Lab Wright-Patterson AFB OH Air Vehicles Directorate.

Lei, J., & Zhong, X. (2012). Linear stability analysis of nose bluntness effects on hypersonic boundary layer transition. *Journal of Spacecraft and Rockets*, *49*(1), 24–37.

Lysenko, V., & Maslov, A. (1981). Transition reversal and one of its causes. *AIAA Journal*, *19*(6), 705–708.

Morkovin, M. V., Reshotko, E., & Herbert, T. (1994). Transition in open flow systemsa reassessment. *Bull. Am. Phys. Soc.*, *39*, 1882.

Mortensen, C. H. (2018). Toward an understanding of supersonic modes in boundary-layer transition for hypersonic flow over blunt cones. *Journal of Fluid Mechanics*, *846*, 789–814.

Saric, W. S., Reed, H. L., & Kerschen, E. J. (2002). Boundary-layer receptivity to freestream disturbances. *Annual review of fluid mechanics*, *34*(1), 291–319.

Softley, E. J. (1968). *Transition of the hypersonic boundary layer on a cone: Part ii. experiments at m= 10 and more on blunt cone transition* (Tech. Rep.). GENERAL ELECTRIC CO PHILADELPHIA PA MISSILE AND SPACE DIV.

Stetson, K. F. (1967). Shock tunnel investigation of boundary-layer transition at m= 5.5. *AIAA J.*, *5*, 899–906.

Visbal, M. R., & Gaitonde, D. V. (2002). On the use of higher-order finite-difference schemes on curvilinear and deforming meshes. *Journal of Computational Physics*, *181*(1), 155–185.

Welch, P. (1967). The use of fast fourier transform for the estimation of power spectra: a method based on time averaging over short, modified periodograms. *IEEE Transactions on audio and electroacoustics*, *15*(2), 70–73.